Lab on a Chip

PAPER

View Article Online
View Journal | View Issue





Cite this: *Lab Chip*, 2017, **17**, 3804

# Probing blood cell mechanics of hematologic processes at the single micron level†

Jordan C. Ciciliano,[a] Reza Abbaspour,[b] Julia Woodall,[c] Caroline Wu,[c] Muhannad S. Bakir[b] and Wilbur A. Lam*[cd]

Received 12th July 2017,
Accepted 16th October 2017

DOI: 10.1039/c7lc00720e

rsc.li/loc

Blood cells circulate in a dynamic fluidic environment, and during hematologic processes such as hemostasis, thrombosis, and inflammation, blood cells interact biophysically with a myriad of vascular matrices—blood clots and the subendothelial matrix. While it is known that adherent cells physiologically respond to the mechanical properties of their underlying matrices, how blood cells interact with their mechanical microenvironment of vascular matrices remains poorly understood. To that end, we developed microfluidic systems that achieve high fidelity, high resolution, single-micron PDMS features that mimic the physical geometries of vascular matrices. With these electron beam lithography (EBL)-based microsystems, the physical interactions of individual blood cells with the mechanical properties of the matrices can be directly visualized. We observe that the physical presence of the matrix, in and of itself, mediates hematologic processes of the three major blood cell types: platelets, erythrocytes, and leukocytes. First, we find that the physical presence of single micron micropillars creates a shear microgradient that is sufficient to cause rapid, localized platelet adhesion and aggregation that leads to complete microchannel occlusion; this response is enhanced with the presence of fibrinogen or collagen on the micropillar surface. Second, we begin to describe the heretofore unknown biophysical parameters for the formation of schistocytes, pathologic erythrocyte fragments associated with various thrombotic microangiopathies (poorly understood, yet life-threatening blood disorders associated with microvascular thrombosis). Finally, we observe that the physical interactions with a vascular matrix is sufficient to cause neutrophils to form procoagulant neutrophil extracellular trap (NET)-like structures. By combining electron beam lithography (EBL), photolithography, and soft lithography, we thus create microfluidic devices that provide novel insight into the response of blood cells to the mechanical microenvironment of vascular matrices and have promise as research-enabling and diagnostic platforms.

## Introduction

While the biochemical aspects of cellular processes have been extensively characterized, it has only recently been shown that cells dynamically sense and respond to biophysical cues such as substrate stiffness and geometrical constraints; physical cues even direct cell differentiation and stem cell lineage.[1,2] Blood exists in the especially rich and dynamic mechanical microenvironment of the cardiovascular system: blood cells experience a wide variety of pressures and shear stresses as they navigate the vasculature, and they also interact with and transit biological matrices such as clots and the subendothelial matrix.[3] In fact, studies are beginning to suggest a role for mechanical stimulus in blood cell response, and have found that red blood cells release ATP during shear mediated deformation and that platelets are both shear activated and attenuate contraction force based on substrate stiffness.[4–6] However, there remains a significant gap in knowledge as to the biophysical effect that the presence of vascular matrices has on platelets, erythrocytes, and leukocytes. These interactions are especially relevant in the context of clotting, whereby the exposure of the subendothelium leads to activation of the clotting cascade and formation of fibrin clots.[7] The biological interactions between fibrin and platelets have been well characterized, but the fibrin matrix also changes the physical environment of the cells, both by changing the fluidic microenvironment and by introducing

[a] *Woodruff School of Mechanical Engineering, Petit Institute for Bioengineering and Bioscience, Georgia Institute of Technology, Atlanta, GA, USA*
[b] *School of Electrical and Computer Engineering, Georgia Institute of Technology, Atlanta, GA, USA*
[c] *Wallace H. Coulter Department of Biomedical Engineering, Georgia Institute of Technology and Emory University, Atlanta, GA, USA*
[d] *Department of Pediatrics, Aflac Cancer Center and Blood Disorders Service of Children's Healthcare of Atlanta and Emory University School of Medicine, Atlanta, GA, USA*

† Electronic supplementary information (ESI) available. See DOI: 10.1039/c7lc00720e

physical barriers with which cells interact.[8–10] Clots also dynamically change: when platelets integrated within the clot contract, the size and architecture of the fibrin matrix changes.[6,11,12] Importantly, the mechanobiological effect of these matrices are also likely to play a pathophysiological role in disease states such as disseminated intravascular coagulation (DIC), a prothrombotic life-threatening complication associated with diseases such as sepsis, cancer, and trauma in which uncontrolled clotting occurs diffusely throughout the circulation.[13] In fact, thrombotic microangiopathies are often initially detected by the presence of mechanically damaged red blood cells on patient blood smears, though the exact underlying mechanism of damage remains unclear.[14] Further, while the integration of neutrophils into clots has been shown to impede clot resolution, the biological basis for their integration is not well understood.[15,16] Thus, while the biochemical pathways implicated in pathological clotting are well established, the ongoing biophysical interactions have previously been technologically infeasible to characterize.

To decouple the biophysical effects of vascular matrices from the biochemical, a suite of PDMS microdevices was designed and fabricated to allow for real-time visualization of single cell/matrix interactions. The matrices that blood cells transit are on the size scale of hundreds of nanometers to single microns, both in terms of pore/gap size and fiber diameter.[17–19] Creating features at the single micron scale using traditional photolithography is non-trivial, so a silicon wafer was templated by electron-beam lithography (EBL) and directly poured with polydimethylsiloxane (PDMS). A standard microfluidic channel can then be bonded atop the array to create a sealed device through which blood components are perfused. EBL has been incorporated into the process flow for creating microfluidic devices in a number of ways, including the direct patterning of PDMS and the creation of a silicon master from which a PDMS master can be made for PDMS to PDMS replica molding.[20,21]

Our EBL-patterned microfluidic systems were designed to recapitulate the interactions of single cells with vascular matrices. A simple, controlled realization of this interaction can be described by the movement of cells through a pillar array with "fiber" size of 900 nm and gap size of 2 μm. These dimensions are on the size scale of physical geometries of diverse vascular matrices and PDMS is of a similar stiffness to fibrin clots, endothelial cell gaps, and splenic slits.[17–19] Micropillar arrays have previously been fabricated both in silicon and PDMS, often to describe the mechanical forces of cells or for the size-based separation of cells.[20–22] To our knowledge, however, no other system describes the interaction of cells and matrices by flowing cells through single micron pillar arrays. Further, we designed a microcanal device to recapitulate the basic physical dimensions of microvascular constrictions that result from *in vivo* pathologies such as microangiopathies. The microdevice canals are 2 μm wide and 3 μm tall, and range in length from 2 μm to 90 μm, thus providing a simplified system in which we can consider cell response to large deformations over time. In these pathologies, the combination of thrombosis and vasoconstriction alters the local flow profile such that blood cells are exposed to large forces as they deform through the physical matrices. There are studies (computational and microfluidics-based) that describe aspects of RBC and neutrophil deformation, but there is not a system that allows for real time visual analysis of blood cell passage through single-micron physical constrictions.[23–27] Using these devices, we then begin to describe the biophysical response of platelets, RBCs, and neutrophils to relevant vascular matrices, in isolation, as well as in conjunction with one another.

## Experimental

### Device fabrication

Devices were created with features on the order of biologically relevant matrices, that is at the single-micron level. As creating high fidelity features of this dimension using traditional photolithography is non-trivial, electron-beam lithography (EBL) was used to create a silicon wafer template that could be used to create microfluidics *via* direct soft lithography with the elastomeric polymer, polydimethylsiloxane (PDMS, Corning). To mitigate the poor silicon to photoresist selectivity for deep etching of the sub-micron features, a layer of $SiO_2$ was deposited *via* plasma-enhanced-vapor-deposition (PECVD) to form a hard mask. Next, a thin layer of electron-beam-lithography (EBL) photoresist was spun on the $SiO_2$ layer and patterned using the EBL tool. Dry-etching transferred the patterned features from the photoresist to the hardmask. The silicon wafer was then etched. While EBL's sequential deep reactive-ion etching (DRIE) and passivation cycles of the Bosch process generally result in side wall roughness (scalloping), an optimized recipe, termed the nano-Bosch process, results in smooth side walls etched in the silicon substrate.[28–30] The resulting feature smoothness is necessary for the successful release of cured PDMS from the master.

Thus, using EBL, a silicon master was patterned with holes to create PDMS pillars (~900 nm diameter and 3 μm height, with a 2 μm gap) or patterned with vias to create PDMS canals (2 μm width and 3 μm height, with lengths varying from 2–90 μm). After patterning, the silicon master was vapor treated with hexamethyldisiloxane (HMDS) to create a hydrophobic substrate that further encourages PDMS release. PDMS (at a 10 : 1 ratio of elastomer to curing agent) was poured over the treated silicon wafer, and the wafer was placed in a vacuum chamber for ~1 hour to ensure PDMS entry into the micron-sized features. PDMS was then cured overnight at 60 °C, before the devices were cut out and the wafer was repoured. The direct EBL-patterned PDMS "feature layer" then serves as the bottom surface of the microfluidic device. To create a closed microfluidic device, PDMS channels were created from silicon wafers templated *via* traditional photolithography and SU-8. Both layer surfaces—

feature and channel—were activated using the handheld Corona Treater (Electro-Technic Products), and the PDMS layers were bonded by aligning the layers by eye under a microscope, placing the layers together, and transferring the bonded device on a hot plate at 80 °C for 10 minutes. The two-part system allows the user to mix and match between micron-sized features and channels to study various systems. For platelet micropillar experiments, the channel was 150 μm wide and 6 μm tall, inlet and outlet holes were punched ~1000 μm apart, and the long axis of the micropillar array was bonded perpendicular to flow direction. For RBC and neutrophil micropillar experiments, the channel was 150 μm wide and 3 μm high. The channel for the microcanal device is 26 μm wide and 3 μm tall, and each canal is approximately centered between inlet and outlet holes. An additional outlet hole was punched downstream of the first outlet hole to create a viewing window of cells post-canal.

### Device characterization

Inspection and characterization of the PDMS features was achieved by scanning electron microscopy (SEM). SEM images confirm that PDMS pillars and canals are of the expected dimensions and fidelity (Fig. 1). We designed our devices and experimental setup such that vessel geometries and flow rates were within biological reason. The fluidic microenvironment of each device was described *via* 2-D COMSOL modeling with an incompressible Newtonian fluid and constant inlet flow rate and atmospheric pressure at the outlet; this gives an estimate of the fluidic microenvironment that the cells are initially exposed to. How this physical microenvironment changes as cells interact with and adhere in the system is outside the scope of this work. For the pillar device, the flow rate is 0.2 μL $min^{-1}$ and the shear rate is maximal between the rows of pillars at ~50 000 $s^{-1}$, with notable dead zones behind the pillars (Fig. 2A). There is no appreciable pressure differential across the pillar array. For the canal device, the flow rate is 0.5 μL $min^{-1}$ and the shear stress is constant throughout the canal at 20 000 dynes per $cm^2$, independent of canal length. The length of the canal does, however, change the pressure drop across the canals. Pressure calculations in the microcanals can also be approximated by modeling microfluidics as circuit.[31] Briefly, Ohm's law,

$$V = IR, \quad (1)$$

where $V$ is voltage, $I$ is current, and $R$ is resistance has an analogue in microfluidics *via* the Hagen Poiseuille law

$$\Delta p = QR_H, \quad (2)$$

where $\Delta p$ is the pressure drop across a channel, $Q$ is flow rate, and $R_H$ is the hydraulic resistance. $R_H$ depends on fluid

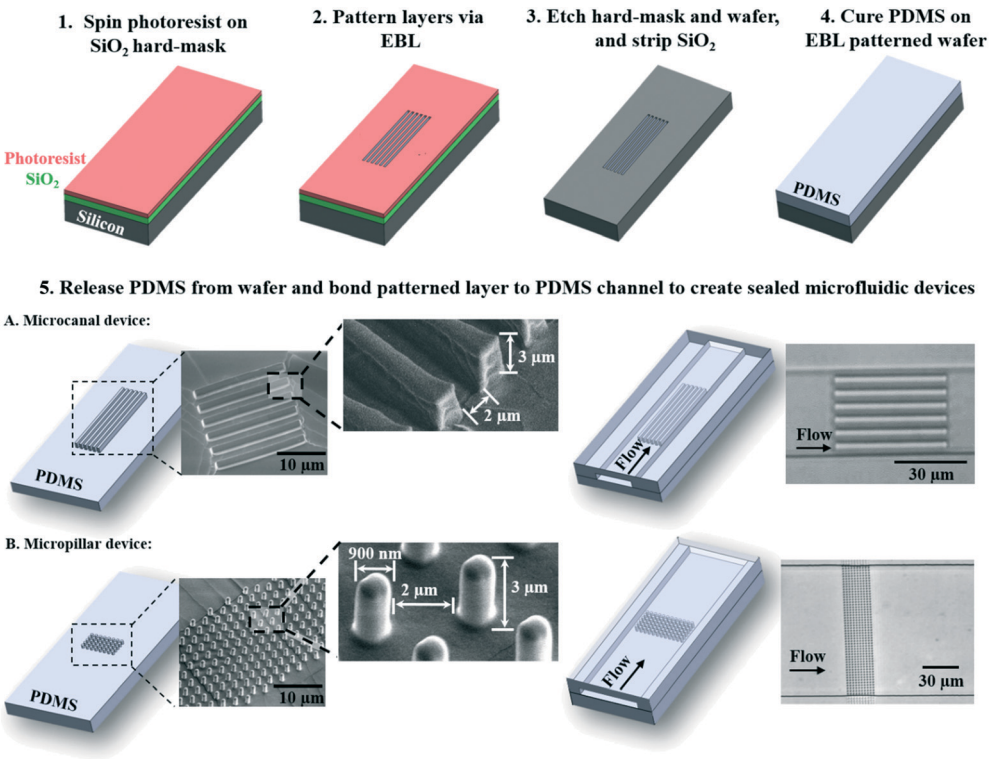


**Fig. 1** Micropillar and microcanal fabrication process flow. (1–3) Pattern a silicon wafer using EBL techniques. (4) Use direct soft lithography to transfer silicon features to cured PDMS. (5) Microfluidic channels created *via* standard photolithography are then bonded to the EBL-patterned features to create two devices: A. microcanal array and B. micropillar array.

 

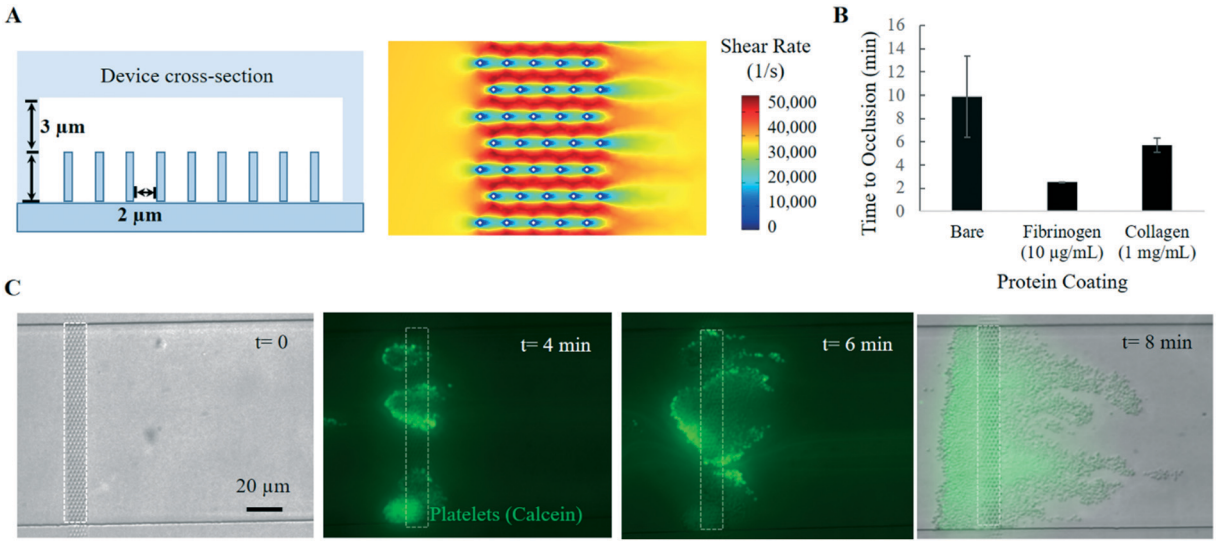


Fig. 2 Platelets adhere in bare and biochemically-coated micropillar devices. A. Cross-section of device that platelets are made to transit (left) and shear environment created by presence of pillars (right). B. Platelets adhere to pillar array and cause channel occlusion. Addition of fibrinogen and collagen enhance aggregation ($N$ = 5 micropillar experiments per condition). C. Time course of platelet adherence and aggregation in a BSA blocked micropillar array (platelets: calcein). Over the course of 8 minutes, the channel becomes fully occluded.

viscosity ($\mu$) and channel width ($w$), height ($h$), and length ($L$). For a channel where $w$–$h$:

$$R_{\mathrm{H}} = \frac{32\mu L(w+h)^4}{\pi(wh)^4}. \quad (3)$$

Pressure drop then varies directly with the length of the microfluidic channel. As in circuits, microfluidic channels in parallel can be added as resistors in parallel:

$$\frac{1}{R_{\mathrm{eq}}} = \frac{1}{R_{\mathrm{H},1}} + \cdots + \frac{1}{R_{\mathrm{H},n}}. \quad (4)$$

The canal fluidic can be treated as a circuit in which there are seven parallel resistors of the same resistance, as the channels have the same width, height, and length. The total resistance, $R_{\mathrm{eq}}$, is

$$R_{\mathrm{H,eq}} = \frac{R_{\mathrm{H}}}{7}. \quad (5)$$

For blood ($\mu$ = 3.2 × $10^{-3}$ Pa s) perfused at a flow rate of $Q$ = 0.5 μL $\mathrm{min}^{-1}$, the pressure drop across microcanals of $w$ = 2 μm, $h$ = 3 μm, and $l$ [μm] is:

$$\Delta p \sim 4.61 \times l \quad [\mathrm{kPa}]. \quad (6)$$

For canal lengths from 10–90 μm, the pressure drop ranges from ~46 kPa to 415 kPa. Pressure drop in the 3 × 3 μm cross-section canal can be found using the same method to be:

$$\Delta p \sim 1.91 \times l \quad [\mathrm{kPa}]. \quad (7)$$

These calculations describe the pressure drop before cells are introduced to the system; also confirmed *via* Comsol modeling. The dynamic pressure environment is complicated by cells alternately plugging and transiting individual canals. If a cell is perfectly blocking one canal, the pressure in the rest of the system increases by a factor of resistance. Thus, if all but one canal is blocked, the pressure drop is 7 times those reported above.

### Adsorbing biomolecular coatings to the PDMS surface

Directly after bonding, all devices were blocked with 3% BSA *via* gravity driven flow. To ensure fully filled, bubble-free channels, a BSA droplet was pipetted over inlet and outlets and devices were placed in vacuum chamber for a 1 hour incubation. Other biologics were introduced to PDMS surface by gravity driven flow and passive adsorption: fibrinogen (10 μg $\mathrm{mL}^{-1}$) or collagen (1 mg $\mathrm{mL}^{-1}$) incubated for 1 hour.

### Collecting and staining human blood samples

Human blood was drawn according to institutional review board-approved protocols per the Declaration of Helsinki, and all subjects gave informed consent. Washed platelets were isolated by centrifugation of whole blood (drawn into ACD) at 150 g for 10 minutes, collecting the supernatant (platelet rich plasma, PRP), adding 10% v/v ACD to the solution, and centrifuging the supernatant at 900 g for 5 minutes. The platelet pellet was then resuspended in Tyrode's buffer containing 0.1% BSA. Platelets were stained with 2 μM calcein AM or anti-CD41 antibody (Novus) at 1 : 200. RBCs were isolated by centrifuging blood (drawn into sodium citrate, Becton Dickson) at 150 g for 10 minutes, discarding the supernatant, and washing 3× with PBS (400 g for 7 minutes). RBCs were resuspended in PBS to ~20% hematocrit unless otherwise noted in order to better visualize single cell fragmentation and to better represent the effective hematocrit in

small vessels. At 40% hematocrit, individual cells at the inlet and the outlet of the canals are not as easily discernible from one another, thus impairing real-time visual analysis of fragmentation. We do not expect a difference in hematocrit between 20 and 40% to result in quantitative fragmentation differences as cells traverse the canals one-by-one regardless of concentration. Staining red blood cells with R18 (Sigma) greatly affected their mechanical stability (data not shown), and thus all RBC studies were performed using bright field microscopy. Neutrophils were isolated from whole blood using MACSxpress® Neutrophil Isolation Kit; neutrophils were then washed in PBS (210 g for 10 minutes) and resuspended in either PBS or PRP. Stains and primary/secondary antibodies were added directly to the cell mixture. Neutrophils were stained with a combination of Hoechst 33342 at 1 : 1000; Sytox Green at 1 : 1000; anti-histone H3 (Abcam, ab5103) at 1 : 200; or anti-elastase (Abcam, ab68672) at 1 : 200. Samples were perfused through microfluidic devices at 0.5 μL $min^{-1}$ using Harvard Apparatus syringe pump.

## Results & discussion

### Physical matrix causes spatially controlled platelet adhesion and aggregation

Shear stress is known to be a biophysical activator of platelets, and the pathological relevance of shear stress is well described, especially as it relates to von Willebrand factor (vWF) mediated clotting and the progression of atherosclerosis.[32–35] Further, it has been found that in the absence of soluble antagonists, a shear stress gradient is sufficient to initiate platelet aggregation.[36–38] In addition, platelets are shown to bind immobilized ligands at different shear rates: the platelet αIIbβ3 integrin binds fibrinogen at low physiological shear rates of 600–900 $s^{-1}$ while the platelet GPIb receptor binds von Willebrand factor (vWF) at 1000–10 000 $s^{-1}$.[39] Studies show that both the magnitude of shear as well as the size of a shear microgradient determines platelet activity.[40] Microfluidics allow for the piecewise study of these questions, and the micropillars create regions of high shear as well as stagnant zones.

The biophysical interaction of platelets with a PDMS matrix (absent biological factors) was recapitulated by the micropillar microfluidic device (Fig. 2). The use of washed platelets allows us to take a reductionist approach and discern the effects of the physical microenvironment on platelets exclusively. Perfusion of washed platelets through the channel results in specific, localized platelet adhesion to the pillars, extensive platelet aggregation, and the formation of an occlusive mass that extends to the edges of the micropillar array (Fig. 2C, Movie S1†). Platelet adhesion initiates exclusively at the pillars and aggregation propagates to the extents of the channel area perpendicular to flow, resulting in channel occlusion and flow cessation. More specifically, platelets form initial tethers between the rows of pillars in the middle and back of the array, and large aggregates primarily form at the back of the pillar array. We further found that a single column of micropillars is sufficient to cause platelet aggregation and channel occlusion (Fig. S1†). In the single column pillar array, platelets aggregate exclusively at the back of the pillar array and continue to adhere to the pillars and one another at the back of the array. As the channel becomes occluded by the aggregate, incoming platelets adhere to the platelet mass and back fill the channel, thus extending the aggregate to the front of the pillar array until the channel is occluded. This suggest that platelets are activated in the high shear region between pillars and aggregate in the low shear region behind the pillars—an aggregation profile that has been shown in the literature.[38] These findings suggest that in the absence of platelet agonists and biological ligands, platelets are activated by the shear microenvironment afforded by the physical presence of "fibers" and that overall, clot formation can propagate due to the mechanical cues of the microenvironment, in and of themselves. Importantly, platelets do not adhere to other locations within the channels, and thus adherence and aggregation do not occur in a channel that does not feature micropillars.

In addition to the biochemical components in clot formation, the geometry of the matrix with which platelets interact also plays a role in platelet adhesion and clot propagation. As expected, passive adsorption of collagen and fibrinogen to the pillar surfaces enhances platelet aggregation, as evidenced by a decrease in time to channel occlusion from 10 min to 6 min and 2 min, respectively, suggesting the synergistic effect of biophysical and biochemical factors in clot propagation (Fig. 2B). There does not appear to be a difference in the profile of platelet adherence or aggregate propagation between the coated arrays and the BSA blocked arrays. This furthers our hypothesis that the biophysical and biochemical factors work in an additive manner to achieve platelet aggregation. Platelets do not adhere in uncoated microcanal devices, perhaps because there is not a region of low shear conducive for platelet adhesion (data not shown). However, when collagen and fibrinogen are introduced to the surface of the microcanal device, platelets aggregate and cause channel occlusion, further suggesting that biophysical and biochemical work in concert in pathologically altered environments. In the canals, platelets adhere both at the front and the middle of the canals, aggregate, and then extend to the back of the canal. Collagen coated channels are fully occluded at 70 ± 9 s and fibrinogen coated channels at 45 ± 6 s. This microfluidic thus gives insight into the biophysical and biochemical aspects of clot formation. Further, we found that platelet adherence initiates and is localized to the pillars, and that the aggregation proceeds specifically along the plane of the pillars, leading us to posit that researchers can specify the location and extent of clots *in vitro* by incorporating micron-sized physical matrices.

### Gap size and residence time associated with cellular deformation in microcanals cause differential RBC fragmentation

RBCs are highly deformable, allowing them to readily transit the 3–4 μm diameter capillaries of the microvasculature, all

 

the while maintaining their oxygen carrying capability in the variety of the shear rates of the vasculature. Mechanical properties of RBCs as well as RBC deformation and mechanical filtration by the spleen have been extensively described.[23,25,27,41–44] However, it is known that RBCs fragment *in vivo* when exposed to mechanical disruptions, as is the case of DIC and in the presence of heart valve implants. Indeed, numerous aberrant RBC morphologies are attributed to mechanical disruptions: dacrocytes/tear drop shaped cells, echinocytes, bite cells, and schistocytes.[45] Clinically, the presence of schistocytes on a peripheral blood smear is used as a diagnostic for DIC as well as thrombotic microangiopathies, such as hemolytic uremia syndrome (HUS), thrombotic thrombocytopenic purpura (TTP), which are characterized by uncontrolled microvascular thrombosis.[46] The clinical presence and enumeration of schistocytes is well documented in medical literature and there are many *in vitro* studies that peripherally mention the presence of schistocytes; however, the mechanism by which RBCs fragment is not well characterized. A carefully conducted SEM study in 1970 reported that schistocytes result when "rapidly moving red cells encounter fine fibrin strands," and the image of "hanged red blood cells" from the study is used extensively in medical literature.[47] It is also known that under certain conditions RBCs rupture, expel their hemoglobin, and become ghost cells—empty, closed membranous sacks; RBCs have been found to hemolyze at fluid–fluid shear interfaces of $>15\,000$ dyn cm$^{-2}$ and at fluid–solid interfaces between 1500 and 3000 dyn cm$^{-2}$. The conditions under which these disparate states of damage result remain unknown.[46] Understanding the biophysical parameter space for RBC damage, fragmentation, and destruction is then of immense interest for improved understanding of disease state as well as for development of diagnostics.

RBCs deform elastically through the micropillar array: RBC morphology changes during transit, but RBCs return to their discoid shape upon matrix exit (Fig. S1†). This suggests that forces (including physical constriction) need to be maintained over a distance to affect plastic deformation of RBCs. To that end, in the microcanal device, RBCs deform through a 2 × 3 μm cross-sectional gap over various lengths. At short canal lengths (<20 μm), RBCs elastically deform through the canal; however, as canal length increases, RBCs emerge progressively more damaged (Fig. 3B). At lengths of ~20 μm, cells emerge from canals as echinocytes—RBCs covered in short, blunt spicules—a reversible morphological change that is indicative of the ATP loss that is expected when RBCs are exposed to shear deformation.[45] At lengths >70 μm, the majority of RBCs emerge as cell debris and ghosts—membranous sacs that have expelled their cytoplasmic load. At interim residence in a deformed state, RBCs emerge in fragmented morphologies such as microspherocytes, or small spherical RBCs indicative of membrane and/or volume loss, and schistocytes (Fig. 3B, Movie S2†). Resulting blood cell morphologies can be described by Giemsa staining of the effluent (Fig. S2†).

Interestingly, preliminary evidence suggests that pathologically altered RBCs from a patient with sickle cell disease (SCD) fragment more readily than RBCs from healthy donors. We perfused sickle RBCs in intermediary canal lengths (35–45 μm) as this was the length scale at which healthy RBCs shifted from transiting the canal undamaged to emerging fragmented. It is known that pathologies can change the ability of RBCs to deform through physical matrices, and our findings suggest that the fragmentation profile of sickle RBCs is shifted: the percentage of damaged sickle RBCs plateaus at ~90% at 40 μm lengths as opposed to 45 μm lengths in the healthy case (Fig. 4B). After transiting the canals, a small percentage of cells (~5%) also appear to emerge sickled, though they enter the array as a normal morphology (Fig. 4A). Whether these cells are irreversibly sickled requires further investigation. While sickle RBCs in these experiments look morphologically "healthy" at the entrance of the canals, they nevertheless sustain more damage as they transit the microcanals. This is supported by findings that sickle RBCs are less deformable (both in the deoxygenated and oxygenated state) than healthy RBCs, and we hypothesize that this reduction in deformability leads to increased damage in our system.[48–50] Our device then suggests that the overall population of sickle RBCs are more susceptible to damage when exposed to biophysical microenvironments that are common to SCD (*e.g.*, vaso-occlusion and cerebral vasculopathies).

If the degree of deformation is reduced by increasing the canal cross section to 3 × 3 μm, RBCs elastically deform for all tested canal lengths (up to 90 μm). An array of 3 × 3 canals of 90 μm is similar in pressure drop to a 2 × 3 array of canals ~40 μm in length; we thus hypothesize that in this system, RBC mechanical damage and fragmentation is due to extended residence time in a constricted state. This is supported by quantifying the percent of damaged cells: even when exposed to pressure drops that cause significant damage in 2 × 3 μm gap devices (40% of cells), all cells passing through the 3 × 3 μm array emerge morphologically unchanged (Fig. 5).

### Mechanical interaction of neutrophils with physical matrices leads to formation of NET-like structures

Neutrophils are the most numerous white blood cell subtype and are a key component of the innate immune system: they are the "first responder" to immune challenges as they migrate to sites of infection and phagocytose pathogens. Likewise, there is a wealth of recent literature that describes the process and mechanisms of neutrophil extracellular trap (NET) formation, a process in which neutrophils release their nuclear material into the extracellular space.[51–54] The resulting meshwork of chromatin and DNA studded with histones and cytotoxic enzymes serves as part of the neutrophil's antimicrobial defense system, as NET entrapped pathogens are exposed to high concentrations of antimicrobial proteins. NETs are released in response to numerous factors, including inflammatory stimuli, contact with pathogens, and chemical

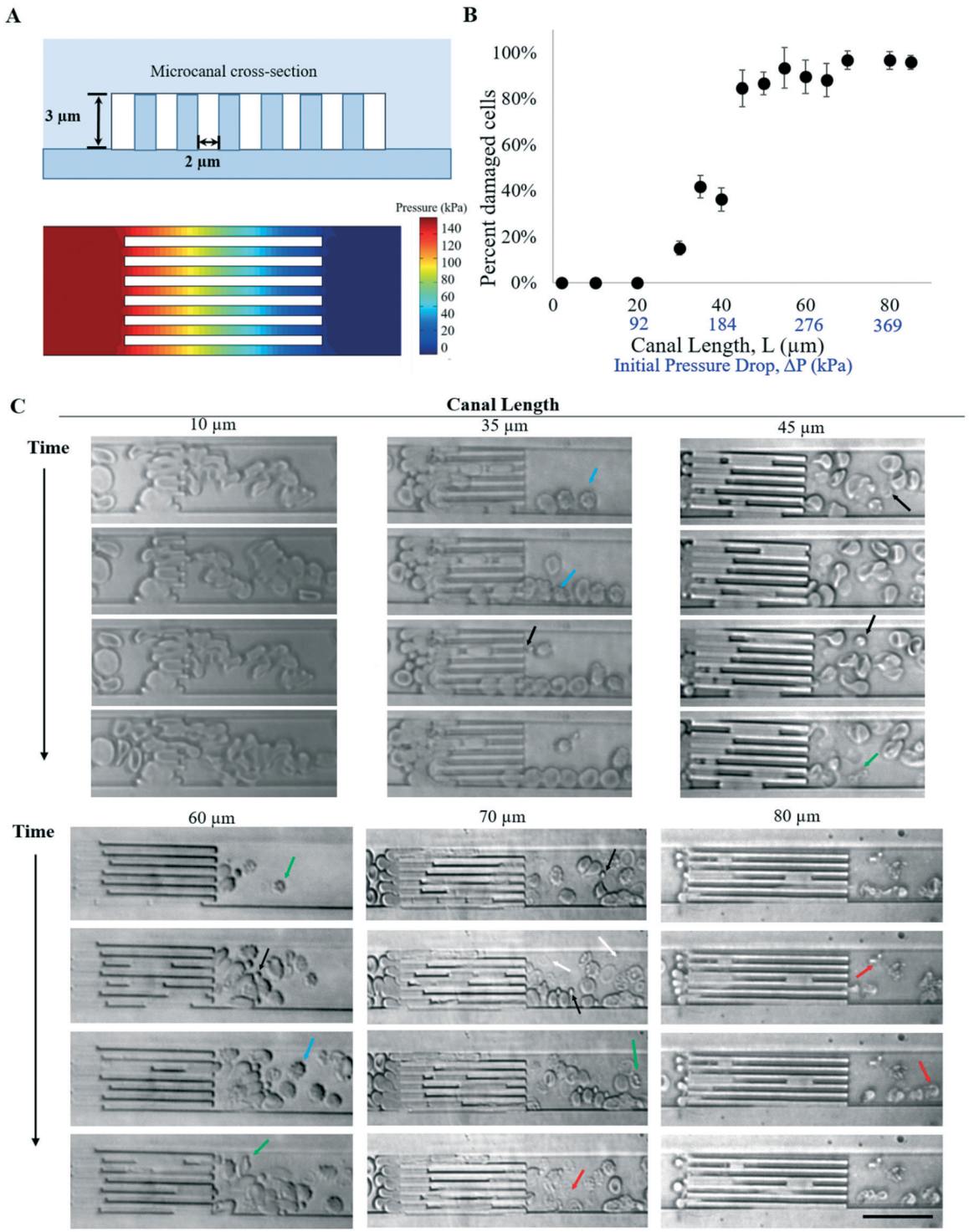


**Fig. 3** As canal length increases, RBCs emerge increasingly damaged. A. Microcanal cross-section and pressure across microcanal device, shown here for canal length of 40 μm. B. As cell length increases, percent of damaged cells increases, plateauing around ~95% starting at 50 μm. C. Representative time lapse images (top panel to bottom panel) of cells traversing canals of lengths from 35–80 μm. As canal lengths increase, severity of damage also increases. Abnormal morphologies are denoted by arrows blue for burr cells, green for schistocytes, black for microspherocytes, white for ghosts, and red for cell debris. Error bar = 20 μm. 200 cells were counted for each experiment and $N > 3$ experiments were performed for each condition.

activation. NETs have also been implicated as a complicating factor in numerous pathologies, including sepsis, cystic fibrosis, and rheumatoid arthritis. Furthermore, *in vivo*, NETs are shown to be procoagulant and to play a role in pathological thrombosis;[15,55,56] however, a recent *in vitro* study suggests that intact NETs do not directly stimulate coagulation, and

 

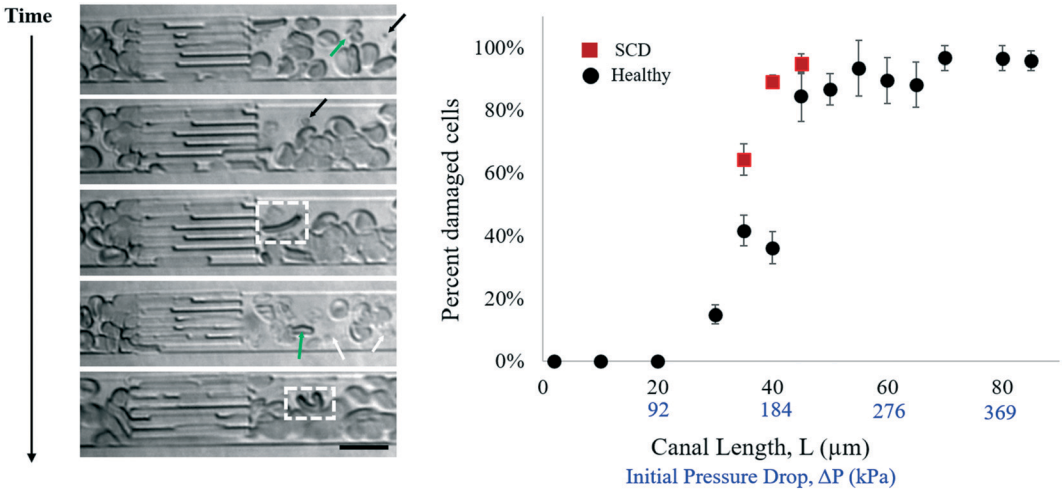


**Fig. 4** SCD RBCs are more readily damaged upon canal transit than are healthy RBCs. Time lapse of sickle red blood cells emerging from 40 μm canals shows various morphological abnormalities, including microspherocytes (black), ghosts (white), and schistocytes (green) (left). A cell appears to be sickled after transit (white dotted box). Scale bar: 20 μm. At the same canal lengths, RBCs from patients with SCD emerge more damaged than RBCs from healthy donors (right). For each SCD experiment, 200 cells were counted, and $N$ = 3 experiments were performed at each length.

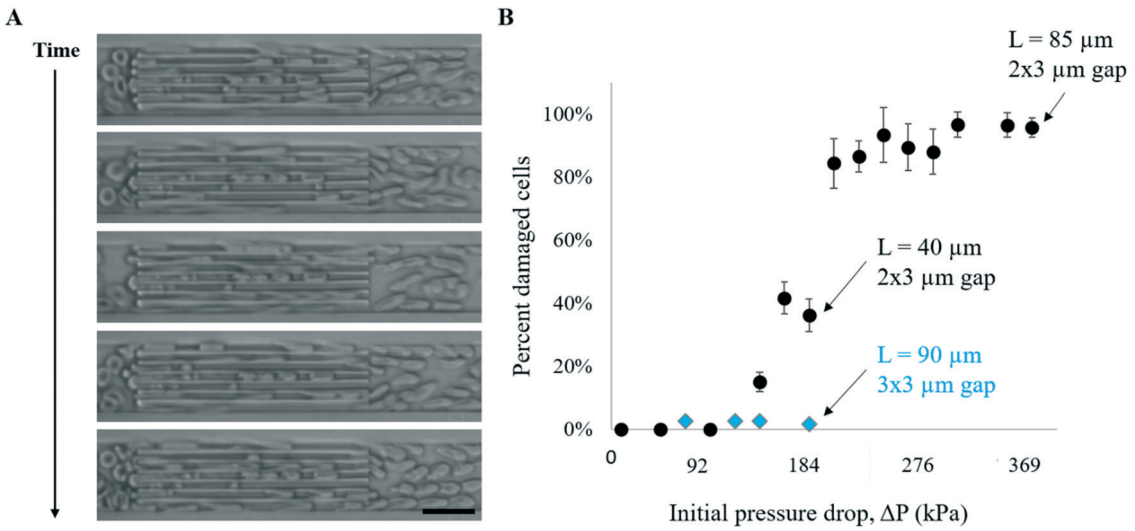


**Fig. 5** RBCs transit 3 × 3 gap without morphological damage. A. Time lapse of RBCs traversing 3 × 3 μm cross section, 90 μm length canals (top to bottom). RBCs emerge with no significant morphology changes. Scale bar is 20 μm. B. At the same initial pressure drop, 40% of RBCs are damaged after transiting a 2 × 3 μm gap (black circles) and ~0% of RBCs are damaged after transiting a 3 × 3 μm gap (blue diamonds).

rather that NET components—histones and neutrophil DNA—are procoagulant.[16] Interestingly, it was reported that mechanical ventilation in patients with respiratory failure can induce neutrophil extracellular trap formation: ventilation results in NETs, but the stimulus is unknown, as bacteria is necessary to recruit neutrophils to the lungs but not to create NETs.[57] These recent reports taken together suggest a role for a mechanical process in the formation of procoagulant "NET-like" structures. Changes in neutrophil mechanics during migration and activation have been described, and Yap and Kamm suggest that microfluidic constrictions can result in neutrophil activation and the formation of pseudopods.[58–60] Recently, a computational study described the fluidization of the neutrophil as it enters a constriction.[61] These studies then give insight into the mechanical activation of neutrophils and further motivates our studies of neutrophil response through single-micron matrices.

We find that when isolated neutrophils interact with the physical matrix of both the micropillar and the microcanal (tested for lengths 5–20 μm), they fragment into stringy, membranous cell fragments (Fig. 6A and S3†). All further neutrophil experiments were performed in 20 μm canals, as this length provides sufficient scaffolding for neutrophil membrane attachment, and thus provides a better platform for the real-time characterization of the membranous neutrophil material and its interactions with other cells. The material adhered to the canals is from a nucleated cell, and not debris, as shown by presence of the membrane impermeable

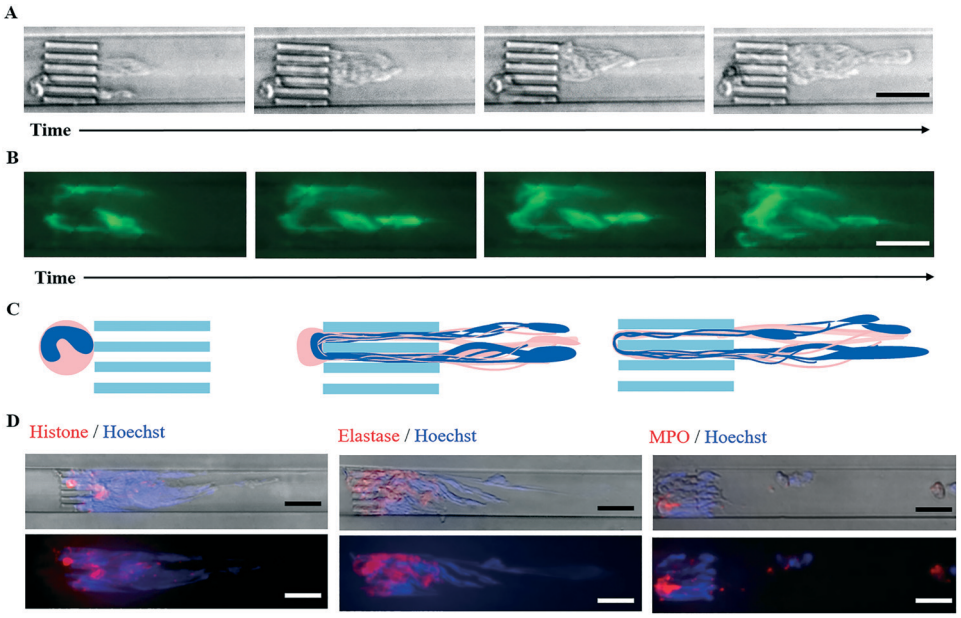


**Fig. 6** Neutrophils mechanically fragment into NET-like material due solely to physical interactions with matrices. A. Neutrophils fragment upon interaction with 20 μm microcanals. As more neutrophils enter the canals, membrane material builds on previously deposited membranes. B. Neutrophil is "dead" and deposited material is DNA rich, as evidenced by staining with the membrane impermeable Sytox Green (green). C. Cartoon schematic of neutrophil interacting with canals. D. Neutrophil material is positive for typical NET components: citrullinated histone H3, elastase, and myeloperoxidase (MPO). Scale bar: 20 μm.

nucleic acid dye, Sytox Green (Fig. 6B). Membranous material is tethered to the canals and accumulates over time as neutrophils are continuously perfused through the device (Fig. 6C, Movie S3†). The resulting cellular material is made up of cell membrane and nuclear material traditionally associated with NETs: DNA (indicated by Hoechst and Sytox Green staining), as well as MPO, elastase, and citrullinated histone H3 (Fig. 6D). The micropillar and microcanal devices demonstrate a variety of shear (50 000–200 000 dyn $cm^{-2}$) and pressure (0–70 kPa) conditions, and we see neutrophil fragmentation in all cases. Both devices do however feature the same constriction geometry: cells traverse a 2 × 3 μm gap. On the other hand, when neutrophils are perfused through channels without micron-sized features (the 26 μm × 3 μm channel), they do not fragment. Likewise, a host of studies show that neutrophils are able to pass through various constriction sizes (on the order of 5 μm) at various pressures (0–30 kPa) without exhibiting the damage shown in our system.[62–64] Due to these factors, we hypothesize that the dimension of the constriction is the critical factor in the creation of NET-like structures.

### Platelet adhesion and RBC entrapment in mechanically induced, NET-like structures

When platelet rich plasma (PRP) enriched with isolated neutrophils is perfused through the microcanals, platelets become entrapped in the stringy neutrophil material. To investigate whether the membranous neutrophil material forms a procoagulant surface we added isolated neutrophils to PRP at ~1 million cells per mL and perfused the mixture through the 20 μL microcanal device. As expected, neutrophils form tethered, membranous material at the microcanals, and platelets adhere specifically to the neutrophil material downstream of the canals (Fig. 7A). There is some colocalization between platelets and histone, elastase, and MPO; with the greatest colocalization between MPO and platelets (Fig. 7B). This shows that the NET components implicated as prothrombotic are present on the surface of the mechanically induced NET-like material. When RBCs and neutrophils are perfused together through the microcanals, RBCs become trapped in the tethered neutrophil membrane. RBCs take on a teardrop shape, whereby they are tethered at one end and elongate with the flow at the other (Fig. 7C, Movie S4†). This suggests that mechanically disrupted neutrophils may also have a role in RBC fragmentation.

## Conclusions

In this work, we leverage microfluidic techniques to create a suite of microfluidic devices that allow for the real-time monitoring of blood cell transit through single-micron matrices that recapitulate the mechanical microenvironment of *in vivo* vascular matrices. Visualization of these specific cellular interactions at this size scale has previously been technologically infeasible. In doing so, we recapitulate the passage of blood cells through physical barriers that are on the single micron scale of biological matrices, while decoupling the effects of the physical presence of a matrix from the biological components of the matrix. Overall, we show that mechanical

 

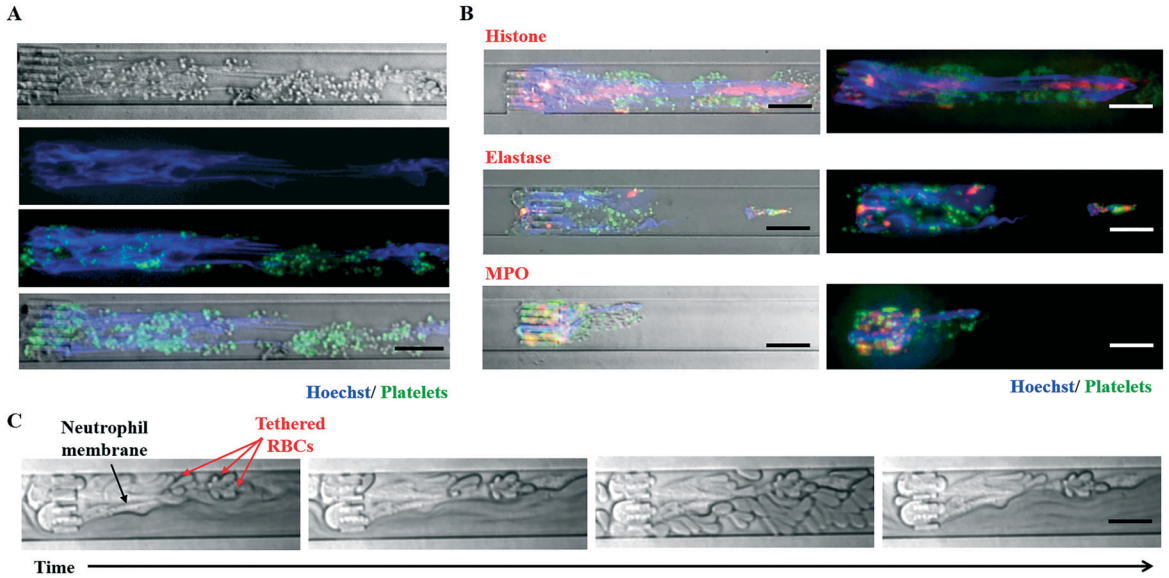


Fig. 7 Platelets and RBCs interact with NET-like material. A. Platelets (CD41, green) adhere to NET-like material (Hoechst, blue). B. Platelets colocalize with NET components and bind elsewhere on membrane. C. RBCs are tethered in neutrophil material. Scale bars: 20 μm.

forces, in and of themselves, have significant, and sometimes surprising, physiologic effects on blood cells. We find that when platelets are perfused through a micropillar array in the absence of agonists or biological ligands, platelets adhere in the array, aggregate, and the mass extends to the edges of the array until the channel is fully occluded – thus the physical properties of vascular matrics are sufficient to initiate or propagate clot formation. It is posited that this spatially localized response to the physical presence of pillars is due to the shear microgradients created by the pillars and the stagnant zones throughout the array. Occlusion of the microchannel is hastened by the synergy between the biophysical and the biochemical when platelet ligands are adsorbed to the micropillars. Extending this technology, additional pillar dimensions and altered pillar stiffness will be studied to further characterize how matrix parameters affect platelet activity. This would inform how disparate architectures and mechanical properties of clots found between healthy and diseased patients can affect the activity of platelets. Furthermore, introduction of additional platelet ligands, such as vWF, will further describe the synergy between biophysical and biochemical cues in platelet aggregation and activation.

In addition, while it is known that RBCs fragment in response to mechanical damage *in vivo*, the mechanism of action of this fragmentation is not well understood. We hypothesized that there is a temporal aspect of membrane remodeling that leads to RBC fragmentation as opposed to hemolysis. To that end, microcanals were designed to probe the deformation of cells through a microconstriction as a function of time in a deformed state. The extent of RBC damage, and thus the resulting morphological abnormality, was found to be dependent on the length of the canal, corresponding both to distance through which cells deform and the pressure differential to which cells are exposed. Reversibly damaged RBCs are primarily seen at short canal lengths, microspherocytes and schistocytes at the intermediate lengths, and ghosts and cell debris at the longest canal lengths. Our findings suggest that pathologically abnormal cells in SCD exhibit a different fragmentation profile than do healthy cells, and that the physical dimension of a constriction determines a cell's fragmentation profile. Interestingly, and consistent with our data, despite their increased stiffness, SCD RBCs are also more fragile and prone to hemolysis, which is also a major hallmark of the disease.[65] Further experiments to more fully define the biophysical parameter space can be accomplished by altering the shear rate (*via* velocity), monitoring morphology changes *via* high speed imaging, and by examining additional pathologically altered cells (malaria infected, deoxygenated SCD, thalassemia). Understanding how these factors alter RBC fragmentation profile will inform pathological processes and create a parameter space for use in developing diagnostic assays.

Finally, although NETs are thought to be created in response to biochemical stimuli caused by a microbial pathogen or an inflammatory response, we show that perfusion of neutrophils through the microcanal device results in "NET-like" membranous structures that are marked by DNA, histone, elastase and MPO. Moreover, this mechanically damaged neutrophil membrane appears to be procoagulant: platelets adhere to the membranous substrate that contains histone, elastase, and MPO. The recent report that NET components, as opposed to intact NETs, are procoagulant, combined with our findings, suggest that mechanical stimuli could be implicated in the prothrombotic role of neutrophils. This neutrophil debris is further able to trap RBCs, at which point RBC membranes undergo deformation that could lead to RBC damage (Fig. 8). Further experiments leveraging this technology will explore the role of neutrophil activation on

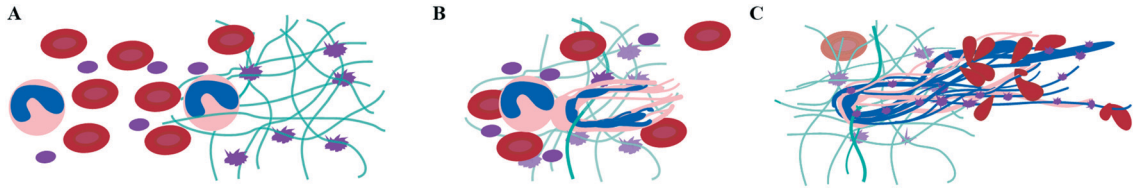


Fig. 8 Schematic of proposed blood cell/matrix interactions. A and B. Our findings suggest that neutrophils become fragmented in a nascent vascular matrix. C. Platelets adhere and RBCs become entrapped in the NET-like material.



mechanically induced "NET" formation, as activated neutrophils are stiffer than resting neutrophils, thus possibly increasing their proclivity for fragmentation in a biophysical matrix. This has direct implications for the role of neutrophils in thrombosis, as well as the links between coagulation and sepsis. By introducing factors that allow us to determine differences and similarities between biochemical NETosis and the mechanically induced "NET-like" structures that are reported here, we will better understand how to target the adverse prothrombotic effects attributed to NETs *in vivo*. Likewise, as other granulocytes have been shown to produce extracellular traps, introduction of other WBC subtypes into our system will inform their role in pathological clotting.[66]

While our system provides insights into the biophysical effects that a matrix has on blood cells, it does also have limitations. We present a simplified representation of physical interactions that could be further strengthened by examining a three-dimensional realization of these matrices. Likewise, smaller pillars that represent fine fibrin strands would allow for red blood cells to fully wrap around the pillars, thereby more aptly recapitulating the cited mechanism of schistocyte formation. Further, as pressure is not being tightly controlled for each cell within our experiments, the exact pressures that induce cell deformation cannot be deduced from this work. Thus, while our techniques do not wholly recapitulate the biophysical matrices that cells interact with, our findings do provide insight into how blood cells respond to the mechanical microenvironment of vascular matrices that are present in the circulation of healthy and diseased individuals. Taken together, our findings suggest that there is a synergy between DIC, thrombotic microangiopathies, hemolytic anemias, and sepsis that may arise in part from mechanical cues, and has roots in the three major cells present in blood. We have thus presented a research enabling technology that has significant implications for understanding the mechanobiology of hematologic processes.

## Conflicts of interest

There are no conflicts to declare.

## Acknowledgements

We would like to acknowledge M. E. Fay for fabrication efforts. This work was performed in part at the Georgia Tech Institute for Electronics and Nanotechnology, a member of the National Nanotechnology Coordinated Infrastructure supported by the National Science Foundation (ECCS-1542174). The authors would like to thank Devin K. Brown and acknowledge that a portion of this research was conducted at the Center for Nanophase Materials Sciences, a DOE Office of Science User Facility. Financial support for this work was provided by: National Science Foundation CAREER Award 1150235 (W. A. L.) and National Institutes of Health grants R01HL121264 (W. A. L.), R01HL130918 (W. A. L.), U01-HL117721 (W. A. L.), and U54HL112309 (W. A. L.).

## References

1 D. E. Discher, P. Janmey and Y. L. Wang, *Science*, 2005, **310**, 1139–1143.
2 D. E. Discher, D. J. Mooney and P. W. Zandstra, *Science*, 2009, **324**, 1673–1677.
3 D. M. Wootton and D. N. Ku, *Annu. Rev. Biomed. Eng.*, 1999, **1**, 299–329.
4 A. M. Forsyth, J. Wan, P. D. Owrutsky, M. Abkarian and H. A. Stone, *Proc. Natl. Acad. Sci. U. S. A.*, 2011, **108**, 10986–10991.
5 J. J. Hathcock, *Arterioscler., Thromb., Vasc. Biol.*, 2006, **26**, 1729–1737.
6 W. A. Lam, O. Chaudhuri, A. Crow, K. D. Webster, T. D. Li, A. Kita, J. Huang and D. A. Fletcher, *Nat. Mater.*, 2011, **10**, 61–66.
7 K. L. Berkner, in *eLS*, John Wiley & Sons, Ltd, 2001, DOI: 10.1038/npg.els.0001408.
8 Y. Qiu, A. C. Brown, D. R. Myers, Y. Sakurai, R. G. Mannino, R. Tran, B. Ahn, E. T. Hardy, M. F. Kee, S. Kumar, G. Bao, T. H. Barker and W. A. Lam, *Proc. Natl. Acad. Sci. U. S. A.*, 2014, **111**, 14430–14435.
9 A. Bonnefoy, Q. Liu, C. Legrand and M. M. Frojmovic, *Biophys. J.*, 2000, **78**, 2834–2843.
10 A. L. Fogelson and K. B. Neeves, *Annu. Rev. Fluid Mech.*, 2015, **47**, 377–403.
11 D. R. Myers, Y. Qiu, M. E. Fay, M. Tennenbaum, D. Chester, J. Cuadrado, Y. Sakurai, J. Baek, R. Tran, J. C. Ciciliano, B. Ahn, R. G. Mannino, S. T. Bunting, C. Bennett, M. Briones, A. Fernandez-Nieves, M. L. Smith, A. C. Brown, T. Sulchek and W. A. Lam, *Nat. Mater.*, 2017, **16**, 230–235.
12 D. B. Cines, T. Lebedeva, C. Nagaswami, V. Hayes, W. Massefski, R. I. Litvinov, L. Rauova, T. J. Lowery and J. W. Weisel, *Blood*, 2014, **123**, 1596–1603.
13 M. Levi and H. Ten Cate, *N. Engl. J. Med.*, 1999, **341**, 586–592.
14 G. Zini, G. d'Onofrio, C. Briggs, W. Erber, J. M. Jou, S. H. Lee, S. McFadden, J. L. Vives-Corrons, N. Yutaka and J. F. Lesesve, *Int. J. Lab. Hematol.*, 2012, **34**, 107–116.

 

15 I. Varju, C. Longstaff, L. Szabo, A. Z. Farkas, V. J. Varga-Szabo, A. Tanka-Salamon, R. Machovich and K. Kolev, *Thromb. Haemostasis*, 2015, **113**, 1289–1298.
16 D. F. Noubouossie, M. F. Whelihan, Y. B. Yu, E. Sparkenbaugh, R. Pawlinski, D. M. Monroe and N. S. Key, *Blood*, 2017, **129**, 1021–1029.
17 B. Blombäck and M. Okada, *Thromb. Res.*, 1982, **25**, 51–70.
18 M. Okada, B. Blombäck, M. D. Chang and B. Horowitz, *J. Biol. Chem.*, 1985, **260**, 1811–1820.
19 I. V. Pivkin, Z. Peng, G. E. Karniadakis, P. A. Buffet, M. Dao and S. Suresh, *Proc. Natl. Acad. Sci. U. S. A.*, 2016, **113**, 7804–7809.
20 M. C. Moolman, Z. Huang, S. T. Krishnan, J. W. Kerssemakers and N. H. Dekker, *J. Nanobiotechnol.*, 2013, **11**, 12.
21 M. T. Russell, L. S. Pingree, M. C. Hersam and T. J. Marks, *Langmuir*, 2006, **22**, 6712–6718.
22 J. Fu, Y. K. Wang, M. T. Yang, R. A. Desai, X. Yu, Z. Liu and C. S. Chen, *Nat. Methods*, 2010, **7**, 733–736.
23 G. Deplaine, I. Safeukui, F. Jeddi, F. Lacoste, V. Brousse, S. Perrot, S. Biligui, M. Guillotte, C. Guitton, S. Dokmak, B. Aussilhou, A. Sauvanet, D. Cazals Hatem, F. Paye, M. Thellier, D. Mazier, G. Milon, N. Mohandas, O. Mercereau-Puijalon, P. H. David and P. A. Buffet, *Blood*, 2011, **117**, e88–e95.
24 S. Guido and G. Tomaiuolo, *C. R. Phys.*, 2009, **10**, 751–763.
25 S. Salehyar and Q. Zhu, *Biomech. Model. Mechanobiol.*, 2017, **16**, 921–931.
26 M. E. Myrand-Lapierre, X. Deng, R. R. Ang, K. Matthews, A. T. Santoso and H. Ma, *Lab Chip*, 2015, **15**, 159–167.
27 Q. Guo, S. P. Duffy, K. Matthews, A. T. Santoso, M. D. Scott and H. Ma, *J. Biomech.*, 2014, **47**, 1767–1776.
28 S. A. McAuley, H. Ashraf, L. Atabo, A. Chambers, S. Hall, J. Hopkins and G. Nicholls, *J. Phys. D: Appl. Phys.*, 2001, **34**, 2769.
29 A. M. Hynes, H. Ashraf, J. K. Bhardwaj, J. Hopkins, I. Johnston and J. N. Shepherd, *Sens. Actuators, A*, 1999, **74**, 13–17.
30 R. Abbaspour, D. K. Brown and M. S. Bakir, *J. Micromech. Microeng.*, 2017, **27**, 025011.
31 K. W. Oh, K. Lee, B. Ahn and E. P. Furlani, *Lab Chip*, 2012, **12**, 515–545.
32 T. A. Doggett, G. Girdhar, A. Lawshe, D. W. Schmidtke, I. J. Laurenzi, S. L. Diamond and T. G. Diacovo, *Biophys. J.*, 2002, **83**, 194–205.
33 N. A. Mody and M. R. King, *Biophys. J.*, 2008, **95**, 2556–2574.
34 Z. S. Kaplan and S. P. Jackson, *Hematology Am. Soc. Hematol. Educ. Program*, 2011, **2011**, 51–61.
35 L. P. Dasi, H. A. Simon, P. Sucosky and A. P. Yoganathan, *Clin. Exp. Pharmacol. Physiol.*, 2009, **36**, 225–237.
36 E. Gutierrez, B. G. Petrich, S. J. Shattil, M. H. Ginsberg, A. Groisman and A. Kasirer-Friede, *Lab Chip*, 2008, **8**, 1486–1495.
37 R. R. Hansen, A. R. Wufsus, S. T. Barton, A. A. Onasoga, R. M. Johnson-Paben and K. B. Neeves, *Ann. Biomed. Eng.*, 2013, **41**, 250–262.
38 W. S. Nesbitt, E. Westein, F. J. Tovar-Lopez, E. Tolouei, A. Mitchell, J. Fu, J. Carberry, A. Fouras and S. P. Jackson, *Nat. Med.*, 2009, **15**, 665–673.
39 B. Savage, E. Saldívar and Z. M. Ruggeri, *Cell*, 1996, **84**, 289–297.
40 W. S. Nesbitt, E. Westein, F. J. Tovar-Lopez, E. Tolouei, A. Mitchell, J. Fu, J. Carberry, A. Fouras and S. P. Jackson, *Nat. Med.*, 2009, **15**, 665–673.
41 J. Picot, P. A. Ndour, S. D. Lefevre, W. El Nemer, H. Tawfik, J. Galimand, L. Da Costa, J. A. Ribeil, M. de Montalembert, V. Brousse, B. Le Pioufle, P. Buffet, C. Le Van Kim and O. Francais, *Am. J. Hematol.*, 2015, **90**, 339–345.
42 N. F. Zeng and W. D. Ristenpart, *Biomicrofluidics*, 2014, **8**, 064123.
43 Y. Park, C. A. Best, T. Auth, N. S. Gov, S. A. Safran, G. Popescu, S. Suresh and M. S. Feld, *Proc. Natl. Acad. Sci. U. S. A.*, 2010, **107**, 1289–1294.
44 J. M. Kwan, Q. Guo, D. L. Kyluik-Price, H. Ma and M. D. Scott, *Am. J. Hematol.*, 2013, **88**, 682–689.
45 B. J. Bain, *Blood Cells: A Practical Guide*, Wiley, 2008.
46 S. H. Orkin and D. G. Nathan, *Nathan and Oski's Hematology of Infancy and Childhood*, Saunders/Elsevier, 2009.
47 B. S. Bull and I. N. Kuhn, *Blood*, 1970, **35**, 104–111.
48 Y. Alapan, Y. Matsuyama, J. A. Little and U. A. Gurkan, *Technology*, 2016, **4**, 71–79.
49 Y. Alapan, J. A. Little and U. A. Gurkan, *Sci. Rep.*, 2014, **4**, 7173.
50 X. Li, M. Dao, G. Lykotrafitis and G. E. Karniadakis, *J. Biomech.*, 2017, **50**, 34–41.
51 V. Brinkmann, U. Reichard, C. Goosmann, B. Fauler, Y. Uhlemann, D. S. Weiss, Y. Weinrauch and A. Zychlinsky, *Science*, 2004, **303**, 1532–1535.
52 M. Zawrotniak and M. Rapala-Kozik, *Acta Biochim. Pol.*, 2013, **60**, 277–284.
53 M. J. Kaplan and M. Radic, *J. Immunol.*, 2012, **189**, 2689–2695.
54 B. G. Yipp, B. Petri, D. Salina, C. N. Jenne, B. N. Scott, L. D. Zbytnuik, K. Pittman, M. Asaduzzaman, K. Wu, H. C. Meijndert, S. E. Malawista, A. de Boisfleury Chevance, K. Zhang, J. Conly and P. Kubes, *Nat. Med.*, 2012, **18**, 1386–1393.
55 T. A. Fuchs, A. Brill, D. Duerschmied, D. Schatzberg, M. Monestier, D. D. Myers Jr, S. K. Wrobleski, T. W. Wakefield, J. H. Hartwig and D. D. Wagner, *Proc. Natl. Acad. Sci. U. S. A.*, 2010, **107**, 15880–15885.
56 B. McDonald, R. P. Davis, S. J. Kim, M. Tse, C. T. Esmon, E. Kolaczkowska and C. N. Jenne, *Blood*, 2017, **129**, 1357–1367.
57 C. Yildiz, N. Palaniyar, G. Otulakowski, M. A. Khan, M. Post, W. M. Kuebler, K. Tanswell, R. Belcastro, A. Masood, D. Engelberts and B. P. Kavanagh, *Anesthesiology*, 2015, **122**, 864–875.
58 B. Yap and R. D. Kamm, *J. Appl. Physiol.*, 2005, **98**, 1930–1939.
59 B. Yap and R. D. Kamm, *J. Appl. Physiol.*, 2005, **99**, 2323–2330.

60 Q. Wang, E. T. Chiang, M. Lim, J. Lai, R. Rogers, P. A. Janmey, D. Shepro and C. M. Doerschuk, *Blood*, 2001, **97**, 660–668.
61 T. Wu and J. J. Feng, *Biophys. J.*, 2015, **109**, 2235–2245.
62 M. E. Fay, D. R. Myers, A. Kumar, C. T. Turbyfield, R. Byler, K. Crawford, R. G. Mannino, A. Laohapant, E. A. Tyburski, Y. Sakurai, M. J. Rosenbluth, N. A. Switz, T. A. Sulchek, M. D. Graham and W. A. Lam, *Proc. Natl. Acad. Sci. U. S. A.*, 2016, **113**, 1987–1992.
63 A. E. Ekpenyong, N. Toepfner, C. Fiddler, M. Herbig, W. Li, G. Cojoc, C. Summers, J. Guck and E. R. Chilvers, *Sci. Adv.*, 2017, **3**, e1602536.
64 A. C. Rowat, D. E. Jaalouk, M. Zwerger, W. L. Ung, I. A. Eydelnant, D. E. Olins, A. L. Olins, H. Herrmann, D. A. Weitz and J. Lammerding, *J. Biol. Chem.*, 2013, **288**, 8610–8618.
65 G. J. Kato, M. H. Steinberg and M. T. Gladwin, *J. Clin. Invest.*, 2017, **127**, 750–760.
66 O. Goldmann and E. Medina, *Front. Immunol.*, 2012, **3**, 420.

 